# Aminated Sodium Lignosulfonate for Efficient Adsorption of Methyl Blue Dye

Li-Zhu Huo , Chaofei Guo , Zhu-Xiang Gong , Hao Xu , Xue-Juan Yang * , Yu-Xuan Wang * , Xi-Ping Luo *

Posted Date: 22 November 2023

doi: 10.20944/preprints202311.1344.v1

Keywords: sodium lignosulfonate; amination; adsorption; dye

*Article*

# Aminated sodium lignosulfonate for efficient adsorption of methyl blue dye

**Li-Zhu Huo †, Chaofei Guo †, Zhu-Xiang Gong; Hao Xu; Xue-Juan Yang * and Yu-Xuan Wang *and Xi-Ping Luo ***

College of Chemistry and Materials Engineering, Zhejiang A&F University, Hangzhou, Zhejiang Province 311300, PR China; hlz@stu.zafu.edu.cn (L.-Z.H); chaoguo@zafu.edu.cn (C.G.); 2022005@stu.zafu.edu.cn (Z.-X.G.); jasonxu@stu.zafu.edu.cn (H.X.)

* Correspondence: yangxj@zafu.edu.cn (X.-J.Y.) 20190050@zafu.edu.cn (Y.-X.W.); luoxiping@zafu.edu.cn (X.- P.L.)

† These authors contributed equally to this work.

**Abstract:** The research aims to resolve water pollution generated by dye wastewater. In this paper, the aminated sodium lignosulfonate (AELS) was prepared through the Mannich reaction, and the synthesis conditions were optimized using orthogonal experiments to determine the best amination conditions. The successful preparation of AELS was demonstrated through the use of FT-IR, XRD, TG, SEM and XPS characterization techniques. Then, the adsorption capacity of Methyl blue (MB) by AELS was compared in a range of different circumstances, like pH, adsorbent dose, initial concentration, time, and temperature. Additionally, the kinetics, isotherms, and thermodynamic properties of the AELS adsorption for MB were studied and discussed. The results indicated that the fitting results were consistent with the pseudo-second-order kinetic model and Langmuir isotherm model, in accordance with the mechanism of single-molecular-layer chemisorption. And the adsorption of MB by AELS was a spontaneous and endothermic process. Upon completion of five adsorption experiments, the adsorption capacity of MB by AELS was determined to be 107.95 mg $g^{-1}$, which was 5.3% lower than the first experiment. This research promotes the effective use of natural resources and allows for the sustainable use of lignin and the advancement of new applications for it.

**Keywords:** sodium lignosulfonate; amination; adsorption; dye

## 1. Introduction

Water is a ubiquitous element on our planet and an essential ingredient for human life. Nonetheless, the growth of industry has led to the release of large amounts of untreated wastewater into the environment, resulting in serious water pollution. Dyes are frequently employed across a wide range of industries including textiles, paper and printing [1]. The composition of dye wastewater is complicated, largely composed of hard-to-degrade organic matter, and containing a high concentration of toxic substances such as aniline, phenols, heavy metals and so on. Each year, approximately 21 tons of toxic dyes are released into the hydrological cycle, causing a serious threat to soil, aquatic life, and humans [2-4].

MB is a heterocyclic compound with an aromatic ring anionic dye. This substance is employed for the staining of protozoa vivax, bacteria, and nerve cells in animal tissues, with toxic and bioaccumulative properties to living organisms and the environment, and may produce a mutagenic effect [5]. Thus, MB needs to be removed, deploying various techniques like membrane separation, chemical oxidation, biodegradation, photocatalysis and adsorption [6-10]. Adsorption is an economical approach out of these methods, which has the benefits of easy operation, affordability and immunity to hazardous pollutants [11,12]. Through this process, the dye is transferred from the aqueous effluent to the solid phase, thus shrinking the effluent volume [13]. Many materials have been reported for the adsorption of MB, such as Mn/MCM-41, PVA/PAA@PDA film, and magnetic $Ni_xMg_{(1-x)}$ $Fe_2O_4$ nanoparticles, etc. [14-16], and very few lignin has been used as MB adsorbent. Due to its economic cost, plentiful supply and biodegradability, lignin is garnering greater attention.

 doi:10.20944/preprints202311.1344.v1



Lignin is the second largest biomass resource in the plant kingdom after cellulose, accounting for about 15-30% of plant cell wall [17,18], and it is estimated that up to 150 billion tons of lignin are produced annually worldwide from plant growth. Lignin, a three-dimensional aromatic polymer, is composed of three phenylpropane units joined by ether bonds and carbon-carbon bonds, such as guaiacyl (G), syringyl (S), and para-hydroxyl (H) [19,20]. It contains many functional groups, such as phenolic hydroxyl, alcohol hydroxyl, carbonyl, carboxyl, methoxy and conjugated double bonds [21].

Sodium lignosulfonate (ELS) is similar with lignin in structure, and a water-soluble sulfonated lignin derivative, with unique three-dimensional network structure. The use of it in adsorption is restricted because of its high solubility. To enhance the application, various modifications can be made. Of those, the Mannich reaction is the most straightforward and convenient, as the amine group can be ionized when exposed to an acidic atmosphere and acquire a positive charge [22]. Hang Chen et al. [23] prepared graphene oxide/aminated sodium Lignosulfonate aerogel (GALA) with three-dimensional structure by photoactivation. And under optimal conditions, the maximum adsorption capacity and removal rate of malachite green (MG) reached 113.5 mg $g^{-1}$ and 91.72%. Within 5 adsorption-desorption cycles maintained 89.8%, which were in accordance with Langmuir model and pseudo-second-order model. Liang liang An et al. [24] synthesized silylated aminated lignin (SAL) in one step and explored its adsorption on Congo red (CR) and Cu(II) in aqueous solution, which involves electrostatic attraction and complexation, Langmuir model and pseudo-second-order model can well describe the adsorption isotherm and kinetic. Research suggests that amination can enhance the adsorption properties of ELS and make it more effective in wastewater treatment. To optimize the modification method, further studies and explorations are required.

In this paper, through Mannich reaction to get AELS by diethylenetriamine (DETA) and formaldehyde (FA). To study the influence of the synthesis conditions for adsorption performance, design and carry out orthogonal experiment to compare the influence of different reaction conditions on the adsorption effect. Characterize the AELS by FT-IR, XRD, TG, SEM and XPS. In addition, compared the adsorption capacity in different pH, adsorbent dose, initial concentration, time and temperature.

## 2. Experiment

### *2.1. Materials*

Sodium Lignosulfonate, diethylenetriamine, 37 wt% formaldehyde solution, sodium hydroxide, hydrochloric acid, isopropyl alcohol, petroleum ether, methyl Blue, deionized water.

### *2.2. Preparation of AELS*

To obtain AELS, add 10 g ELS into a 0.5 mol $L^{-1}$ sodium hydroxide solution, stirring until completely dissolved. Then add DETA and mix well, increase the temperature and slowly add FA, and condensation reflux reaction. After the reaction, the AELS solution was adjusted to acidic with 1 mol $L^{-1}$ hydrochloric acid until no brown precipitate precipitated. The precipitate was washed with isopropanol and petroleum ether for several times, and then washed with deionized water until the filtrate was colorless to obtain AELS products. After that, orthogonal experiments were used to determine the optimal conditions for amination of ELS.

### *2.3. Adsorption Experiment*

A certain dose of AELS was added to 25 mL of dye and oscillated at constant temperature for a certain time. After the adsorption, the absorbance of the dye was measured at the maximum absorption wavelength by Ultraviolet spectrophotometer, and the adsorption capacity $q_e$ (mg $g^{-1}$), $q_t$ (mg $g^{-1}$) and removal rate R (%) were calculated according to the following formula:

$$q_e = \frac{C_0 - C_e}{M} \times V \quad (1)$$

$$q_t = \frac{C_0 - C_t}{M} \times V \quad (2)$$

$$R = \frac{C_0 - C_e}{C_e} \times 100\% \quad (3)$$

 doi:10.20944/preprints202311.1344.v1



In the formula: $q_e$ is the adsorption capacity (mg $g^{-1}$) when the adsorption reaches equilibrium; $q_t$ is the adsorption capacity (mg $g^{-1}$) at the time of t; R is the removal rate at adsorption equilibrium; $C_0$ is the initial concentration of dye (mg $L^{-1}$); $C_t$ is the dye concentration (mg $L^{-1}$) at the time of t; $C_e$ is the dye concentration (mg $L^{-1}$) after adsorption equilibrium; V is the solution volume (L); M is the adsorbent mass (g).

## 3. Result Discussion

### *3.1. Synthesis and Structural Analysis of AELS*

#### 3.1.1. Analysis of AELS Orthogonal Experiments

Under alkaline conditions, the $C_5$ position of ELS, activated by phenolic hydroxyl groups, losed a proton to become a carbon positive ion. DETA and FA undergoed an addition reaction, and reacted with the activated ELS to obtain AELS [25]. Through orthogonal experiment to obtain the optimal condition, the removal rate of every experiment was shown in Table **Table 1.** Analysis table of orthogonal experiment results. According to the R value, the influence degree of temperature, time, amount of DETA and amount of FA on amination of ELS in the reaction was: amount of DETA > amount of FA > temperature > time. The optimal amination condition was $A_4B_3C_1D_4$, i.e., temperature 85 °C, time 4 h, 3 g of DETA, and 4.5 mL of FA. In subsequent experiments, AELS was prepared using this condition.

**Table 1.** Analysis table of orthogonal experiment results.

| Experimental sequence number | Temperature (℃) | Time (h) | DETA quality (g) | HCHO quality (mL) | Removal rate % |
|---|---|---|---|---|---|
| 1 | 55 | 2 | 3 | 1.5 | 40 |
| 2 | 55 | 3 | 6 | 2.5 | 52 |
| 3 | 55 | 4 | 9 | 3.5 | 25 |
| 4 | 55 | 5 | 12 | 4.5 | 43 |
| 5 | 65 | 2 | 6 | 3.5 | 81 |
| 6 | 65 | 3 | 3 | 4.5 | 90 |
| 7 | 65 | 4 | 12 | 1.5 | 38 |
| 8 | 65 | 5 | 9 | 2.5 | 38 |
| 9 | 75 | 2 | 9 | 4.5 | 31 |
| 10 | 75 | 3 | 12 | 3.5 | 34 |
| 11 | 75 | 4 | 3 | 2.5 | 97 |
| 12 | 75 | 5 | 6 | 1.5 | 49 |
| 13 | 85 | 2 | 12 | 2.5 | 55 |
| 14 | 85 | 3 | 9 | 1.5 | 23 |

Preprints (www.preprints.org) | NOT PEER-REVIEWED | Posted: 22 November 2023 doi:10.20944/preprints202311.1344.v1



| | | | | | |
|---|---|---|---|---|---|
| 15 | 85 | 4 | 6 | 4.5 | 91 |
| 16 | 85 | 5 | 3 | 3.5 | 94 |
| $K_1$ | 160 | 207 | 321 | 150 | |
| $K_2$ | 247 | 199 | 273 | 242 | |
| $K_3$ | 211 | 251 | 117 | 234 | |
| $K_4$ | 263 | 224 | 170 | 255 | |
| $k_1$ | 40 | 51.75 | 80.25 | 37.5 | |
| $k_2$ | 61.75 | 49.75 | 68.25 | 60.5 | |
| $k_3$ | 52.75 | 62.75 | 29.25 | 58.5 | |
| $k_4$ | 65.75 | 56 | 42.5 | 63.75 | |
| R | 25.75 | 13 | 51 | 26.25 | |
| Factor primary and secondary order | C> D > A >B | | | | |
| Optimal level | $A_4$ | $B_3$ | $C_1$ | $D_4$ | |
| Optimal combination | $A_4B_3C_1D_4$ | | | | |

3.1.2. Sample Characterization

FT-IR was used to obtain the chemical composition of AELS. As illustrated in Figure **Figure 1.** **a**) FT-IR images of ELS and AELS; (**b**) XRD images of ELS and AELS; (**c**) TG images of ELS and AELS, the FT-IR spectra remained nearly the same prior to and after amination. In both ELS and AELS, the hydroxyl stretching vibration was seen at 3430 $cm^{-1}$, the -$CH_3$ and -$CH_2$ asymmetric stretching vibration was observed at 2940 $cm^{-1}$, the -$CH_3$ and -$CH_2$ symmetric stretching vibration was at 2860 $cm^{-1}$, and the -$SO_3H$ was indicated by a peak at 1040 $cm^{-1}$[26,27]. Following the amination modification, a new vibrational absorption peak at 1630 $cm^{-1}$, which indicatived of the N-H in-plane bending vibration in $NH_2$[28]. The C-N stretching vibration peak at 1350 $cm^{-1}$ in C-$NH_2$ and the C-N stretching vibration peak at 1090 $cm^{-1}$. These peaks indicated that AELS possesses -$NH_2$, -NH and C-N groups. XRD was employed to evaluate the phase of ELS and AELS. As can be seen in Figure **Figure 1.** **a**) FT-IR images of ELS and AELS; (**b**) XRD images of ELS and AELS; (**c**) TG images of ELS and AELS, there were sharp peaks at 22°, 31° and 33° in ELS. However, after amination modification, these peaks vanished, demonstrating the conversion of AELS from its original crystalline structure to an amorphous structure. TG was used to study the thermal stability of ELS and AELS. From Figure **Figure 1.** **a**) FT-IR images of ELS and AELS; (**b**) XRD images of ELS and AELS; (**c**) TG images of ELS and AELS and Table **Table 2.** The TG of ELS and AELS, ELS had a temperature of 166 °C at 5% loss of mass, while AELS had a temperature of 88 °C at 5% loss of mass. Similarly, ELS had a temperature of 677 °C at 50% loss of mass, while AELS had a temperature of 480 °C at 50% loss of mass. These results clearly indicated that AELS was different from ELS thermal stability.

Preprints (www.preprints.org) | NOT PEER-REVIEWED | Posted: 22 November 2023 doi:10.20944/preprints202311.1344.v1



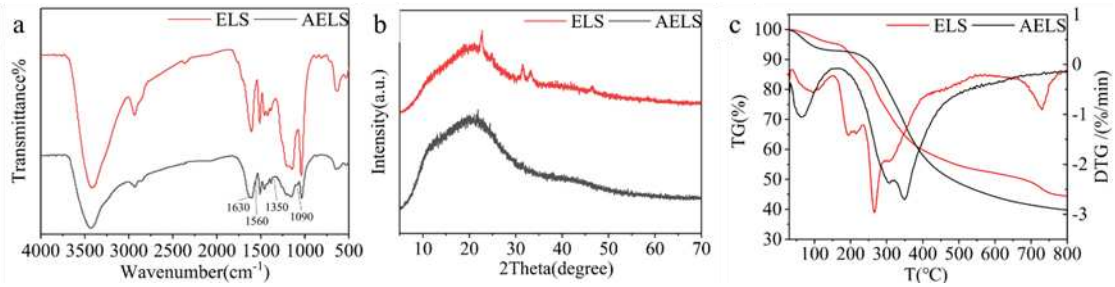


**Figure 1. a**) FT-IR images of ELS and AELS; (**b**) XRD images of ELS and AELS; (**c**) TG images of ELS and AELS.

**Table 2.** The TG of ELS and AELS.

| | Mass loss of 5% at temperature(°C) | Mass loss of 50% at temperature(°C) | Residual amount at 800(°C) |
|---|---|---|---|
| ELS | 166 | 677 | 44.39 |
| AELS | 88 | 480 | 39.76 |

SEM was used to observe the surface topography of the ELS and AELS. As illustrated in Figure

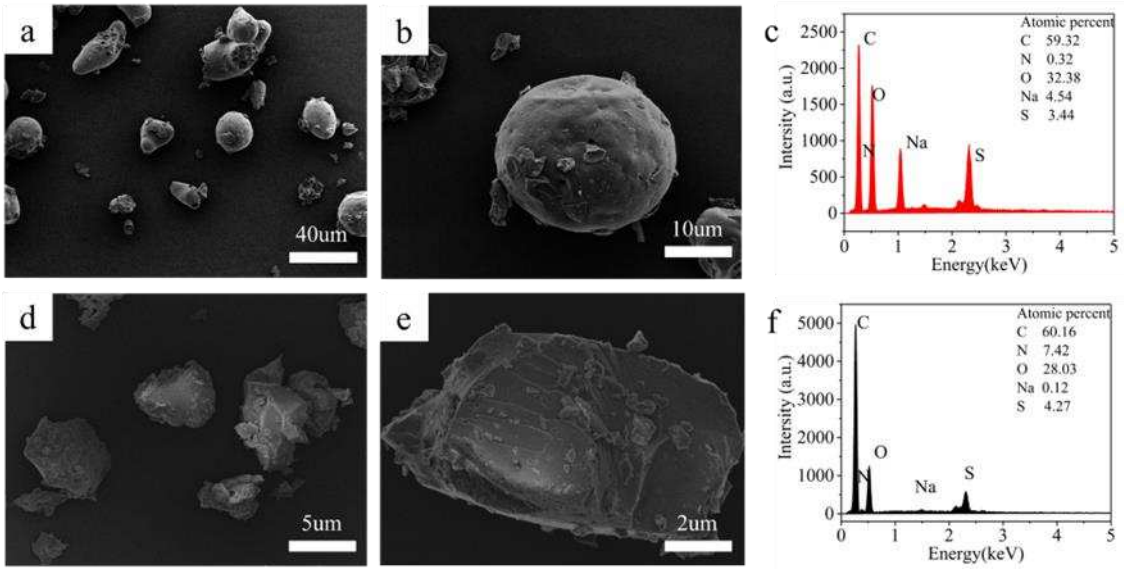


**Figure 2. a)(b**) SEM images of ELS at different magnifications; (**c**) EDS images of ELS; (**d**)(**e**) SEM images of AELS at different magnifications; (**f**) EDS images of AELS, there were many spherical and irregular structures in ELS, and AELS was block structure. Additionally, Figure

Preprints (www.preprints.org) | NOT PEER-REVIEWED | Posted: 22 November 2023 doi:10.20944/preprints202311.1344.v1



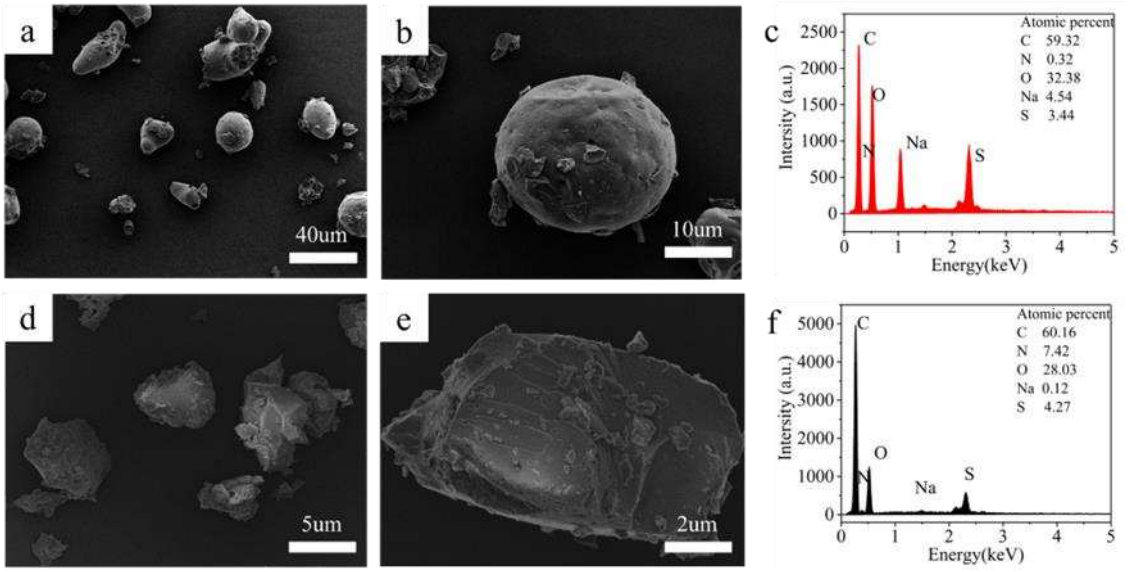


**Figure 2. a**)(**b**) SEM images of ELS at different magnifications; (**c**) EDS images of ELS; (**d**)(**e**) SEM images of AELS at different magnifications; (**f**) EDS images of AELS demonstrated a growth in elemental N in AELS. In order to determine the chemical composition of ELS and AELS, which were tested using XPS and high resolution of N, C, and O shown in Figure **Figure 3. a) XPS** measurement spectra of ELS and AELS; (**b**) high-resolution XPS N spectra; (**c**) high-resolution XPS C spectra; (**d**) high-resolution XPS O spectra. In Figure **Figure 3. a**) XPS measurement spectra of ELS and AELS; (**b**) high-resolution XPS N spectra; (**c**) high-resolution XPS C spectra; (**d**) high-resolution XPS O spectra, both ELS and AELS displayed two main peaks at 284 eV and 531 eV, corresponding to C 1s and O 1s, respectively [29]. As shown in Figure **Figure 3. a**) XPS measurement spectra of ELS and AELS; (**b**) high-resolution XPS N spectra; (**c**) high-resolution XPS C spectra; (**d**) high-resolution XPS O spectra, a new -NH peak becomed visible at 401 eV accompanied by a rise in -$NH_2$ intensity at 399 eV. Denoting an addition of N elemental content after the amination reaction, which was in consonance with the EDS results. The C/O ratio increased because of the introduction of amine groups with alkyl groups on the carbon chain of lignin, resulting in higher carbon and oxygen content [30], in agreement with the EDS results. In contrast to ELS, there were four peaks in the C spectrum and two peaks in the O spectrum of AELS. These changes in both N, C and O spectra after modification indicating that the amine groups were successfully grafted onto ELS. These changes indicated the successful preparation of AELS.

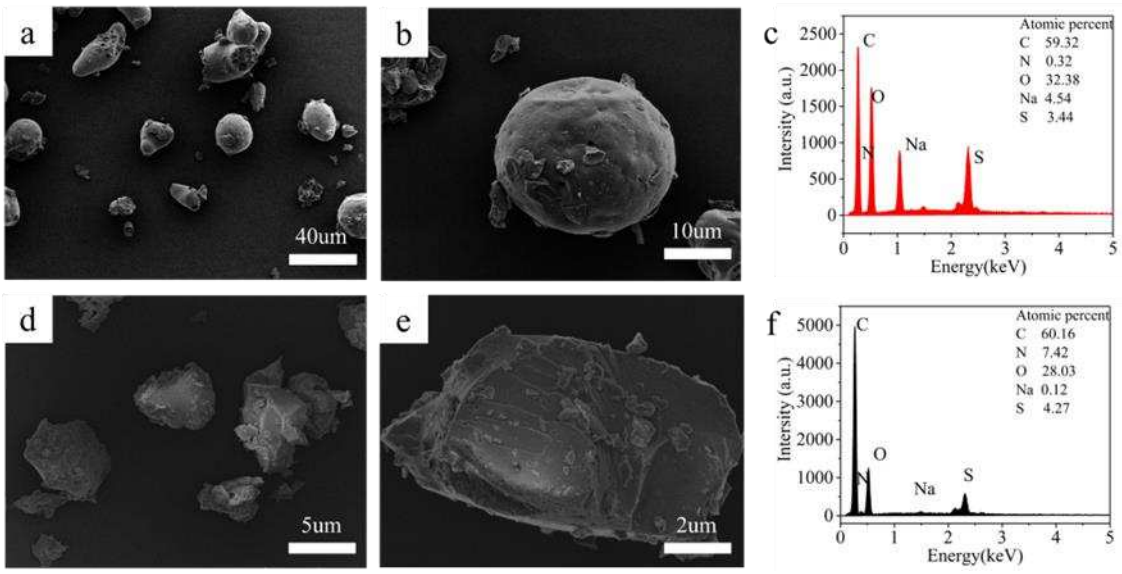

Preprints (www.preprints.org) | NOT PEER-REVIEWED | Posted: 22 November 2023 doi:10.20944/preprints202311.1344.v1



**Figure 2. a**)(**b**) SEM images of ELS at different magnifications; (**c**) EDS images of ELS; (**d**)(**e**) SEM images of AELS at different magnifications; (**f**) EDS images of AELS.

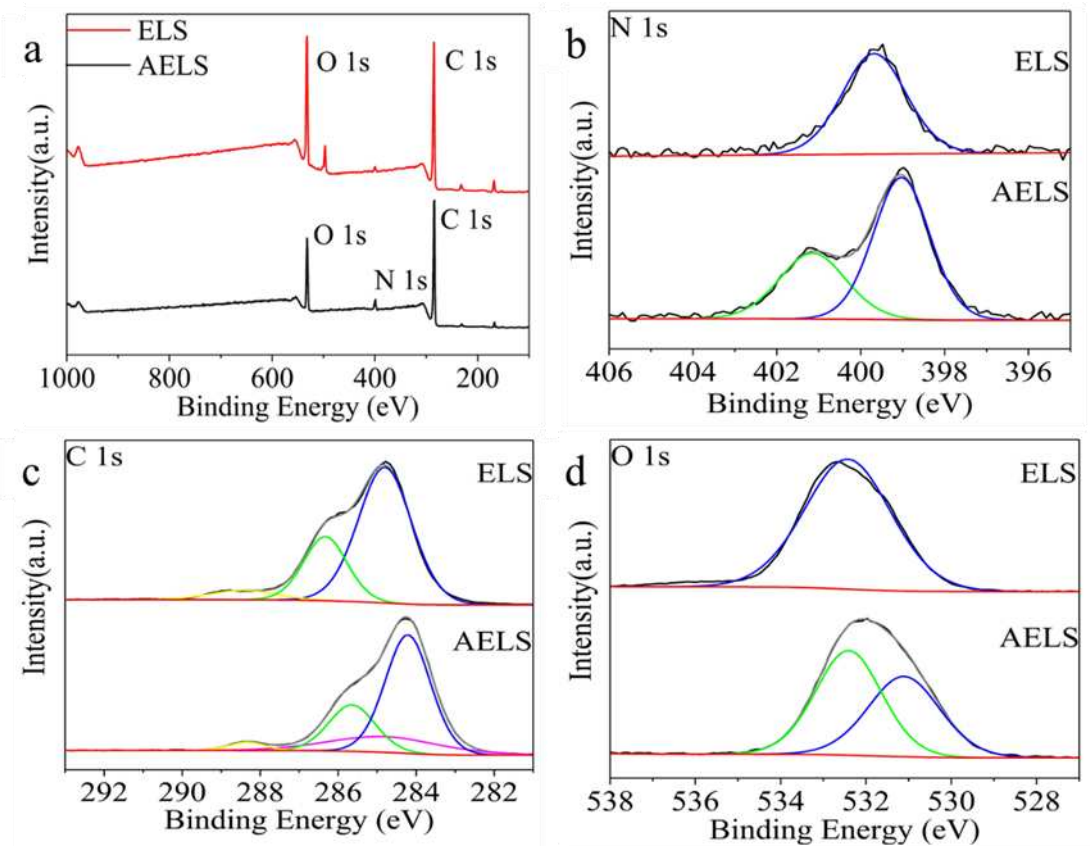


**Figure 3. a**) XPS measurement spectra of ELS and AELS; (**b**) high-resolution XPS N spectra; (**c**) high-resolution XPS C spectra; (**d**) high-resolution XPS O spectra.

*3.2. Performance of AELS Adsorption MB*

pH plays an important role in adsorption and can influence the adsorption capacity through the ionization of functional group of absorbent [31,32]. The effect of pH on MB adsorption was investigated in the range of pH of 3-10 while keeping the initial concentration of MB and temperature constant, as shown in Figure **Figure 4. a**) Influence of different pH on adsorption capacity; (**b**) Effect of adsorption dose on MB adsorption capacity and removal rate. As is evident from the figure, the adsorption capacity decreased with the increase of initial pH. At a pH of 3, the adsorption capacity was 118.13 mg $g^{-1}$. The adsorption mechanism diagram was shown in Figure **Figure 5.** Diagram of adsorption mechanism. With a low pH, AELS was protonated to create amino groups and the active surface was given a positive charge, which then strengthened the electrostatic attraction between the MB molecules and the AELS surface, leading to the diffusion of MB molecules [33]. The presence of the -OH group on AELS and N atoms of MB molecules encouraged hydrogen bonding, which further aids adsorption, culminating in the attainment of adsorption equilibrium. When the pH was high, the AELS potential gradually decreased, the electrostatic attraction with MB molecules decreased, and the presence of -OH would compete with MB. So, the adsorption capacity decreased [34]. At an original dye pH of 6, which was not much different from the adsorption with a pH of 3. So, the pH of MB was not changed in the subsequent experiments.

Preprints (www.preprints.org) | NOT PEER-REVIEWED | Posted: 22 November 2023 doi:10.20944/preprints202311.1344.v1



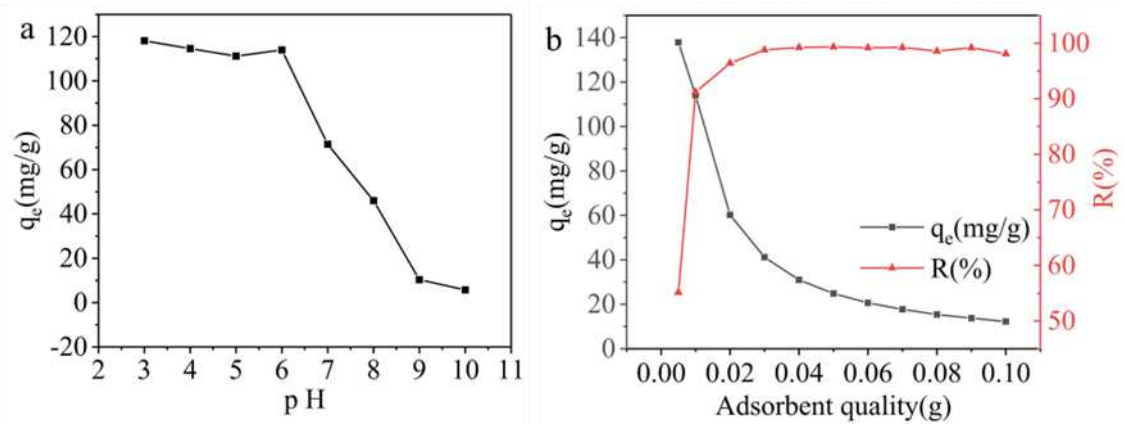


**Figure 4. a**) Influence of different pH on adsorption capacity; (**b**) Effect of adsorption dose on MB adsorption capacity and removal rate.

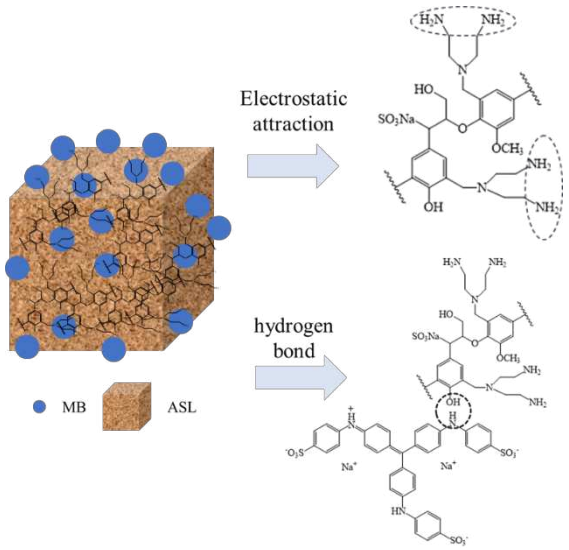


**Figure 5.** Diagram of adsorption mechanism.

The adsorbent dose is also an important parameter and can affect the adsorption capacity and removal rate. The result of effect of adsorbent dose about adsorption capacity and removal rate was shown in Figure **Figure 4. a**) Influence of different pH on adsorption capacity; (**b**) Effect of adsorption dose on MB adsorption capacity and removal rate. From the figure, it can be seen that with the increase of adsorbent dose from 0.005 g to 0.1 g, the adsorption capacity gradually decreased from 113.99 mg $g^{-1}$ to 12.26 mg $g^{-1}$, the removal rate increased from 43% to 99%, the adsorption was gradually saturated and the solution was gradually clarified. The rise in adsorbent dose increased the total surface area and the number of surface-active sites, thus bettering the potential for hydrogen bonding. Nonetheless, the amount of dye molecules in the solution remains constant, causing some of the active sites to not reach full adsorption. Thus, adsorption capacity goes down with the rise of adsorbent and removal increases with the rise of adsorbent. So, the most desirable adsorbent dose was 0.01 g.

The relationship between adsorption capacity and time was shown in Figure **Figure 6.** (**a**) Relationship between time and adsorption capacity; (**b**) AELS adsorption of MB pseudo-first-order kinetic fitting; (**c**) AELS adsorption of MB pseudo-second-order kinetic fitting; (**d**) AELS adsorption of MB intra-particle diffusion kinetic fitting. The adsorption capacity increased rapidly at the initial stage and then increased slowly and eventually reached equilibrium. This because, there were a large number of active sites existing on the surface at the initial stage of adsorption. However, the number of active sites on the surface of AELS was finite. With the extension of the adsorption time, the active

Preprints (www.preprints.org) | NOT PEER-REVIEWED | Posted: 22 November 2023 doi:10.20944/preprints202311.1344.v1



sites gradually saturated, the adsorption rate decreased, and finally reached the adsorption equilibrium [35].

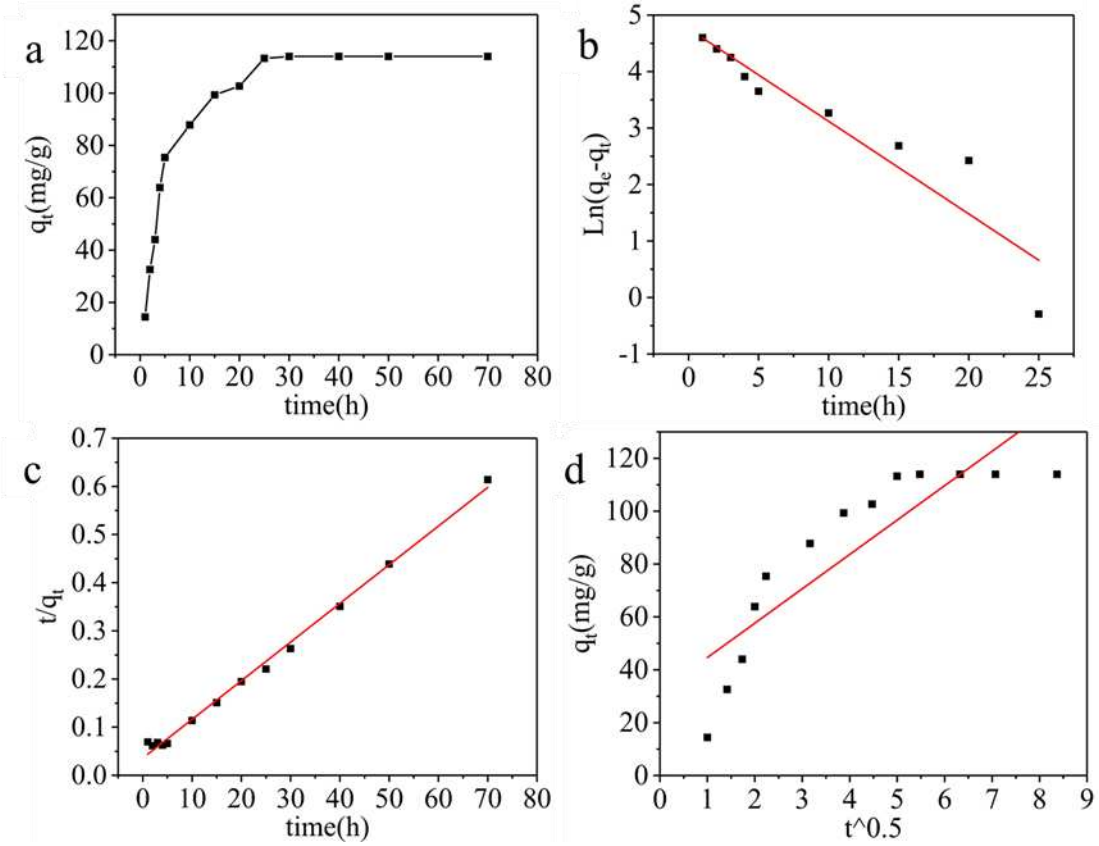


**Figure 6.** (**a**) Relationship between time and adsorption capacity; (**b**) AELS adsorption of MB pseudo-first-order kinetic fitting; (**c**) AELS adsorption of MB pseudo-second-order kinetic fitting; (**d**) AELS adsorption of MB intra-particle diffusion kinetic fitting.

The kinetic model is an essential tool in the simulation of the adsorption process. The pseudo-first-order kinetic model, pseudo-second-order kinetic model and intra-particle diffusion model were employed to fit the experimental data [36-38], and the linear equations were shown as (4), (5) and (6):

$$\ln(q_e - q_t) = \ln q_e - \ln q_t \quad (4)$$

$$\frac{t}{q_t} = \frac{1}{k_2 q_e^2} + \frac{t}{q_e} \quad (5)$$

$$q_t = k_p t^{1/2} + C \quad (6)$$

Where, $k_1$ is the pseudo-first-order kinetic constant ($min^{-1}$), $k_2$ is the pseudo-second-order kinetic constant ($g\ mg^{-1}\ min^{-1}$), $K_p$ is the intra-particle diffusion kinetic constant ($mg\ g^{-1}\ min^{-1/2}$), and C is the boundary thickness correlation constant. The value of C can determine whether the adsorption process is controlled only by intra-particle diffusion. When C=0, the intra-particle diffusion is the only rate-controlling step in the adsorption process; otherwise, the adsorption is not only controlled by intra-particle diffusion, but also involves complex mechanistic processes, including chemical-physical adsorption and boundary layer control.

The fitting of the pseudo-first-order kinetic, pseudo-second-order kinetic, and intra-particle diffusion models were shown in Figure **Figure 6. (a)** Relationship between time and adsorption capacity; (**b**) AELS adsorption of MB pseudo-first-order kinetic fitting; (**c**) AELS adsorption of MB pseudo-second-order kinetic fitting; (**d**) AELS adsorption of MB intra-particle diffusion kinetic fitting, and the linear equation parameters shown in Table

 doi:10.20944/preprints202311.1344.v1



. As demonstrated in the figure, the pseudo-second-order kinetic model was a good fit for the experimental data of MB adsorption onto AELS, with an R-squared value of 0.9948. This suggested that the adsorption of MB by AELS was a result of chemisorption taking place through the sharing or exchange of valence electrons between the AELS surface and the active binding site of MB [39]. As Table

demonstrated, the pseudo-first-order kinetic R-squared value was 0.8691, the intra-particle diffusion R-squared value was 0.7419, and C not being equal to 0, implied that the adsorption process was not only driven by intra-particle diffusion, but also by external mass transfer. The analysis above showed that the adsorption process of AELS on MB followed a pseudo-second-order kinetic model, suggesting that the adsorption process was regulated by the chemisorption mechanism [40].

**Table 3.** Pseudo-first-order kinetics, pseudo-second-order kinetics and intra-particle diffusion fitting parameters.

| **Dynamic model** | **Pseudo-first-order kinetics** | | **Pseudo-second-order kinetics** | | **Intra-particle diffusion** | |
|---|---|---|---|---|---|---|
| Parameters | $R^2$ | 0.8691 | $R^2$ | 0.9948 | $R^2$ | 0.7419 |
| | $K_1$ | 0.1639 | $K_2$ | 0.0016 | $K_p$ | 13.0059 |
| | q | 116.70 | q | 124.53 | C | 31.64 |

The relationship between adsorption capacity and initial concentration and temperature was shown in Figure **Figure 7.** (**a**) Effect of initial concentration of dye on adsorption capacity; (**b**) AELS adsorption of MB Langmuir isotherm fitting; (**c**) AELS adsorption of MB Freundlich isotherm fitting; (**d**) AELS adsorption of MB Temkin isotherm fitting. It can be seen that with the increase of initial concentration and temperature, the adsorption capacity increased and eventually reached equilibrium. This because, a higher concentration gradient was conducive to MB migration, and improved the resistance barrier between solid and aqueous phases, which was the driving force of overcoming mass transfer [41]. With the increase of temperature, the mobility of adsorbate increased, improving the accessibility of adsorbent adsorption sites and dye molecules [42].

Preprints (www.preprints.org) | NOT PEER-REVIEWED | Posted: 22 November 2023 doi:10.20944/preprints202311.1344.v1



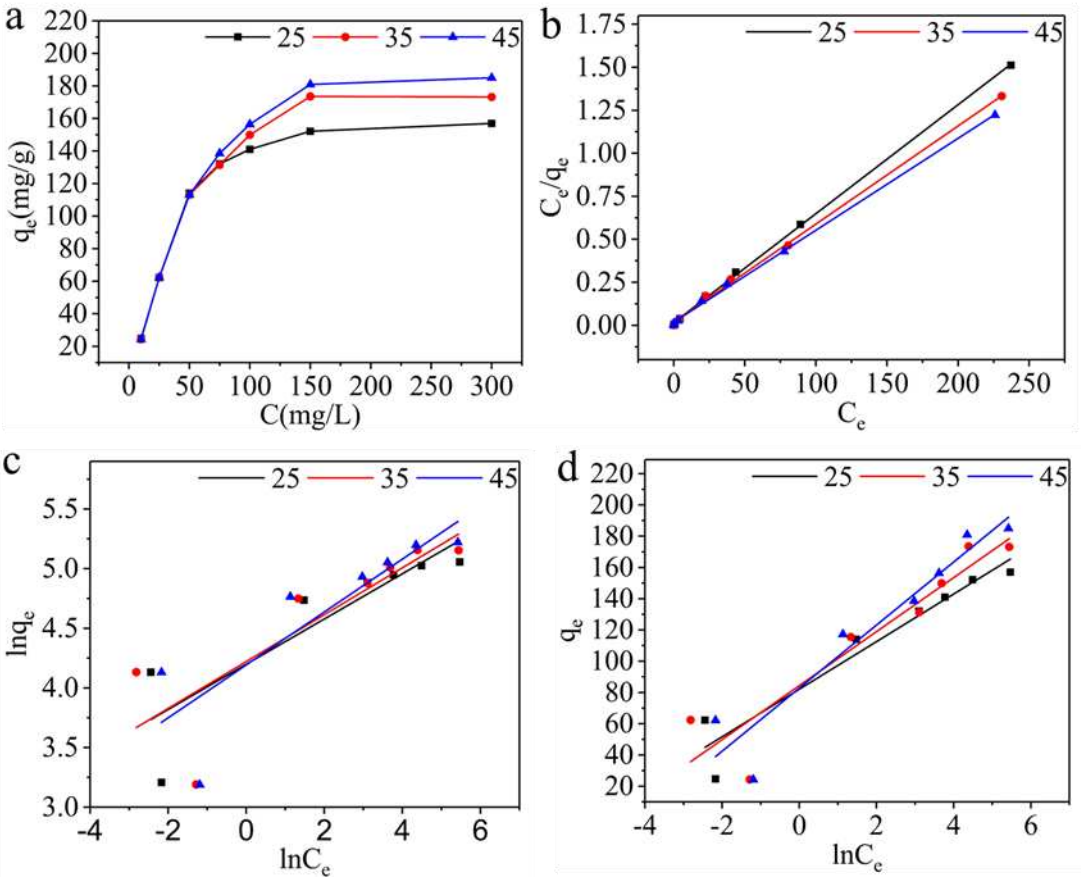


**Figure 7.** (**a**) Effect of initial concentration of dye on adsorption capacity; (**b**) AELS adsorption of MB Langmuir isotherm fitting; (**c**) AELS adsorption of MB Freundlich isotherm fitting; (**d**) AELS adsorption of MB Temkin isotherm fitting.

Adsorption isotherms can reflect the relationship between the adsorption capacity of the adsorbent at equilibrium and the equilibrium concentration of adsorbate in the solution at a specific temperature. Herein, Langmuir, Freundlich and Temkin isotherm models were used to fit the experimental data [43-45], and the linear equations were shown in (7), (8), and (9):

$$\frac{C_e}{q_e} = \frac{C_e}{q_{max}} + \frac{1}{K_L q_{max}} \quad (7)$$

$$\ln q_e = \ln K_F + \frac{1}{n} \ln C_e \quad (8)$$

$$q_e = \frac{RT}{b} \ln A + \frac{RT}{b} \ln C_e \quad (9)$$

Where: $C_e$ (mg $g^{-1}$) is the concentration of the adsorbent at equilibrium; $K_L$ (L $mg^{-1}$) is a Langmuir constant related to the maximum adsorption capacity and adsorption energy. $q_{max}$ (mg $g^{-1}$) is the maximum adsorption capacity of the absorbent; $K_F$ (L $mg^{-1}$) and 1/n are adsorption performance constants and relative adsorption strength parameters related to Freundlich model, respectively; The value of 1/n is generally between 0 and 1, and the magnitude of its value indicates the strength of the effect of concentration on the amount of adsorption; b (J $mol^{-1}$) is heat of adsorption, A (L $mg^{-1}$) is the equilibrium binding constant of Temkin model.

The fitting results of the Langmuir, Freundlich and Temkin adsorption isotherm models were shown in Figure **Figure 7. (a)** Effect of initial concentration of dye on adsorption capacity; (**b**) AELS adsorption of MB Langmuir isotherm fitting; (**c**) AELS adsorption of MB Freundlich isotherm fitting; (**d**) AELS adsorption of MB Temkin isotherm fitting, and the linear equation parameters shown in Table Error! Reference source not found.. As demonstrated in the figure, the Langmuir isotherm model was a good fit for the experimental data of MB adsorption onto AELS, with an R-squared value of 0.9948. This suggested that the adsorption of MB by AELS was monolayer adsorption. As Table **Error! Reference source not found.** demonstrated, the R-squared values of the other two models

Preprints (www.preprints.org) | NOT PEER-REVIEWED | Posted: 22 November 2023 doi:10.20944/preprints202311.1344.v1



were 0.7383 and 0.9147, respectively, which were lower than the R-squared value of the Langmuir isotherm model. Moreover, the maximum adsorption capacity obtained from Langmuir isotherm model was closer to the maximum adsorption capacity obtained by experiment. The results showed that the Langmuir isotherm model could describe the equilibrium well.

**Table 4.** Langmuir, Freundlich and Temkin fitting parameters.

| T/K | Langmuir | | | Freundlich | | | Temkin | | |
|---|---|---|---|---|---|---|---|---|---|
| | $q_m$ (mg g$^{-1}$) | $K_L$ (L mg$^{-1}$) | $R^2$ | $K_F$ (L mg$^{-1}$) | 1/n | $R^2$ | b (J mol$^{-1}$) | A (L mg$^{-1}$) | $R^2$ |
| 298K | 157.73 | 0.42 | 0.9994 | 66.58 | 0.1897 | 0.7383 | 162.75 | 219.54 | 0.9147 |
| 303K | 175.44 | 0.32 | 0.9986 | 68.10 | 0.1965 | 0.6416 | 144.81 | 132.08 | 0.8461 |
| 313K | 187.27 | 0.29 | 0.9987 | 66.20 | 0.2218 | 0.6827 | 129.04 | 60.61 | 0.8887 |

The influence of temperature for adsorption capacity was investigated, the result shown in Figure **Figure 7.** (**a**) Effect of initial concentration of dye on adsorption capacity; (**b**) AELS adsorption of MB Langmuir isotherm fitting; (**c**) AELS adsorption of MB Freundlich isotherm fitting; (**d**) AELS adsorption of MB Temkin isotherm fitting. From the figure, it can be seen that with the increase of temperature the adsorption capacity increases. The relevant thermodynamic parameters were calculated using the following equations:

$$\Delta G^0 = \Delta H^0 - T\Delta S^0 \quad (10)$$

$$\ln(q_e/C_e) = \frac{\Delta S^0}{R} - \frac{\Delta H^0}{RT} \quad (11)$$

Where: $\Delta G^0$ (KJ mol$^{-1}$) is the Gibbs free energy, $\Delta S^0$ (J mol$^{-1}$ K$^{-1}$) is the entropy change, and $\Delta H^0$ (KJ mol$^{-1}$) is the enthalpy change.

The fitting results of the thermodynamic was shown in Figure **Figure 8.** (**a**)Thermodynamic fitting diagram; (**b**) adsorption and regeneration performance, and the linear equation parameters shown in Table **.**

. From the table, it can be seen that $\Delta H^0$ and $\Delta S^0$ were both positive and $\Delta G^0$ was negative. $\Delta H^0 > 0$ indicated that the heat-absorbing nature of the adsorption [46], and $\Delta G^0$ at 25, 35 and 45 ℃ was less than 0, which indicated that adsorption was a spontaneous process. With the increase of temperature, $\Delta G^0$ was getting smaller and smaller, indicating that higher temperature was favorable for adsorption.

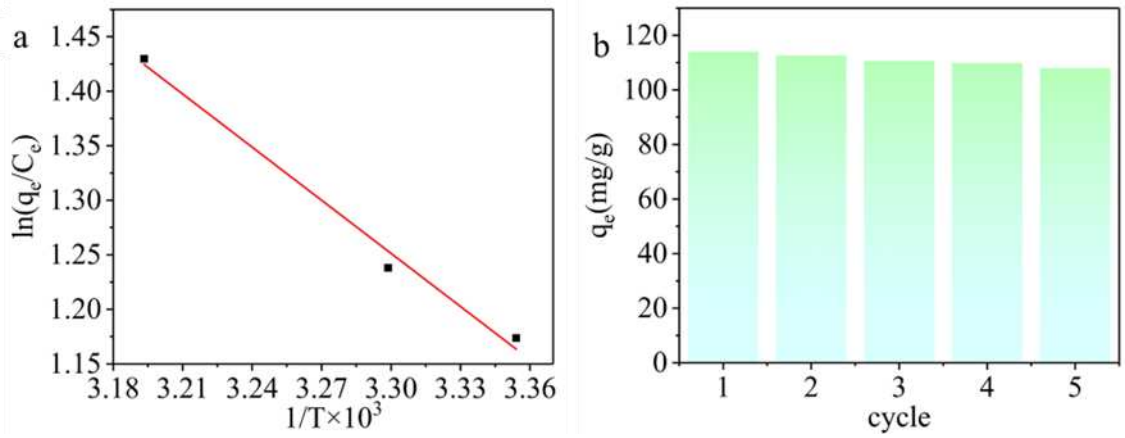


**Figure 8.** (**a**)Thermodynamic fitting diagram; (**b**) adsorption and regeneration performance.

 doi:10.20944/preprints202311.1344.v1



**Table 5.** Thermodynamic fitting parameters.

| Thermodynamic parameter | $\Delta H^0$ (KJ mol$^{-1}$) | $\Delta S^0$ (J mol$^{-1}$ K$^{-1}$) | $\Delta G^0$ (KJ mol$^{-1}$) | | |
|---|---|---|---|---|---|
| | | | 298(K) | 303(K) | 313(K) |
| MB | 13.49 | 54.95 | -16.36 | -16.64 | -17.19 |

To decrease the cost of wastewater treatment, it is essential for recyclability of adsorbent. So, investigated the recyclability of AELS adsorption for MB, the result was shown in Figure **Figure 8.** (**a**)Thermodynamic fitting diagram; (**b**) adsorption and regeneration performance. From the figure, it can be seen that after five adsorption experiments, the adsorption capacity decreased from 113.99 mg g$^{-1}$ to 107.95 mg g$^{-1}$. This because, the irreversible binding of some functional groups in AELS would result in the lowering of adsorption sites, which caused the decrease of the adsorption capacity of AELS. The decrease of about 5.3 percent indicated the reusability of AELS.

## 4. Conclusions

In this study, the ELS was successfully aminated by Mannich reaction and used as the absorbent for adsorption MB. In the adsorption experiments, we observed that the adsorption capacity decreased as the pH and adsorbent dose increased. We found that the adsorption isotherm followed the Langmuir model, while the adsorption kinetics fitted the pseudo-second-order kinetic model. The R-squared values for these models were 0.9948 and 0.9994, respectively. This indicated that the adsorption process involves monomolecular-layer chemisorption. Furthermore, the regeneration of the adsorption material suggested that AELS can be reused.

**Author Contributions:** Conceptualization, L.-Z.H., X.-P.L., C.G. and Y.-X.W.; methodology, L.-Z.H. and Z.-X.G.; software, L.-Z.H.; validation, L.-Z.H. and Z.-X.G.; formal analysis, H.X.; investigation, L.-Z.H.; resources, L.-Z.H., X.-P.L., C.G. and Y.-X.W.; data curation, L.-Z.H. and Z.-X.G.; writing—original draft preparation, L.-Z.H.; writing—review and editing, L.-Z.H., X.-P.L., C.G. and Y.-X.W.; visualization, L.-Z.H.; supervision, H.X; project administration, L.-Z.H., X.-P.L., C.G. and Y.-X.W.; funding acquisition, X.-P.L. All authors have read and agreed to the published version of the manuscript.

**Funding:** This research was funded by the Central Financial Funds for the Forestry Science and Technology Promotion Application Project in China and the Key Research & Development Projects of Zhejiang Province (NO2023TS01 and 2020C03090), the "Pioneer" and "Leading Goose" R&D Program of Zhejiang (2022C02023).

**Conflicts of Interest:** The authors declare no conflict of interest.

## References

1. Ghedjemis, A.; Ayeche, R.; Kebaili, M.; Benouadah, A.; Gil, L.F. Application of natural hydroxyapatite in the treatment of polluted water: Utilization of dromedary bone as bioadsorbent. *Int. J. Appl. Ceram. Technol.* **2022**, 19, 2124-2134. DOI: 10.1111/ijac.14041.
2. Mon, M.; Bruno, R.; Ferrando-Soria, J.; Armentano, D.; Pardo, E. Metal–organic framework technologies for water remediation: towards a sustainable ecosystem. *J. Mater. Chem. A*. **2018**, 6, 4912-4947. DOI: 10.1039/c8ta00264a.
3. Das, T.R.; Patra, S.; Madhuri, R.; Sharma, P.K. Bismuth oxide decorated graphene oxide nanocomposites synthesized via sonochemical assisted hydrothermal method for adsorption of cationic organic dyes. *J. Colloid Interface Sci*. **2018**, 509, 82-93. DOI: 10.1016/j.jcis.2017.08.102
4. Carneiro, P.A.; Umbuzeiro, G.A.; Oliveira, D.P.; Zanoni, M.V.B. Assessment of water contamination caused by a mutagenic textile effluent/dyehouse effluent bearing disperse dyes. *J. Hazard. Mater*. **2010**, 174, 694-699. DOI: 10.1016/j.jhazmat.2009.09.106.

5. Sharma, P.; Hussain, N.; Borah, D.J.; Das, M.R. Kinetics and Adsorption Behavior of the Methyl Blue at the Graphene Oxide/Reduced Graphene Oxide Nanosheet–Water Interface: A Comparative Study. *J. Chem. Eng. Data*. **2013**, 58, 3477-3488. DOI: 10.1021/je400743r.
6. Yang, J.Q.; Monnot, M.; Ercolei, L.; Moulin, P. Membrane-Based Processes Used in Municipal Wastewater Treatment for Water Reuse: State-of-the-Art and Performance Analysis. *Membranes*. **2020**, 10, 131. DOI: 10.3390/membranes10060131.
7. Saravanan, A.; Deivayanai, V.C.; Kumar, P.S.; Rangasamy, G.; Hemavathy, R.V.; Harshana, T.; Gayathri, N.; Alagumalai, K. A detailed review on advanced oxidation process in treatment of wastewater: Mechanism, challenges and future outlook. *Chemosphere*. **2022**, 308, 136524. DOI: 10.1016/j.chemosphere.2022.136524.
8. Pavithra, K.G.; Kumar, P.S.; Jaikumar, V.; Rajan, P.S. Removal of colorants from wastewater: A review on sources and treatment strategies. *J. Ind. Eng. Chem*. **2019**, 75, 1-19. DOI: 10.1016/j.jiec.2019.02.011.
9. Crespo-Monteiro, N.; Cazier, A.; Vocanson, F.; Lefkir, Y.; Reynaud, S.; Michalon, J.Y.; Kämpfe, T.; Destouches, N.; Jourlin, Y. Microstructuring of Mesoporous Titania Films Loaded with Silver Salts to Enhance the Photocatalytic Degradation of Methyl Blue under Visible Light. *Nanomaterials*. **2017**, 7, 334. DOI: 10.3390/nano7100334.
10. Chen, B.; Zhao, H.N.; Chen, S.J.; Long, F.X.; Huang, B.; Yang, B.Y.; Pan, X.J. A magnetically recyclable chitosan composite adsorbent functionalized with EDTA for simultaneous capture of anionic dye and heavy metals in complex wastewater. *Chem. Eng. J*. **2019**, 356, 69-80. DOI: 10.1016/j.cej.2018.08.222.
11. Cao, J.S.; Lin, J.X.; Fang, F.; Zhang, M.T.; Hu, Z.R. A new absorbent by modifying walnut shell for the removal of anionic dye: Kinetic and thermodynamic studies. *Bioresour. Technol*. **2014**, 163, 199-205. DOI: 10.1016/j.biortech.2014.04.046.
12. Yagub, M.T.; Sen, T.K.; Afroze, S.; Ang, H.M. Dye and its removal from aqueous solution by adsorption: A review. *Adv. Colloid Interface Sci*. **2014**, 209, 172-184. DOI: 10.1016/j.cis.2014.04.002.
13. Malarvizhi, R.; Ho, Y.S. The influence of pH and the structure of the dye molecules on adsorption isotherm modeling using activated carbon. *Desalination*. **2010**, 264, 97-101. DOI: 10.1016/j.desal.2010.07.010.
14. Shao, Y.M.; Wang, X.; Kang, Y.; Shu, Y.H.; Sun, Q.Q.; Li, L.S. Application of Mn/MCM-41 as an adsorbent to remove methyl blue from aqueous solution. *J. Colloid Interface Sci*. **2014**, 429, 25-33. DOI: 10.1016/j.jcis.2014.05.004.
15. Yan, J.J.; Huang, Y.P.; Miao, Y.E.; Tjiu, W.W.; Liu, T.X. Polydopamine-coated electrospun poly (vinyl alcohol)/poly (acrylic acid) membranes as efficient dye adsorbent with good recyclability. *J. Hazard. Mater*. **2015**, 283, 730-739. DOI: 10.1016/j.jhazmat.2014.10.040.
16. Li, Y.; Wang, T.C.; Zhang, S.S.; Zhang, Y.L.; Yu, L.L.; Liu, R.J. Adsorption and electrochemical behavior investigation of methyl blue onto magnetic nickel-magnesium ferrites prepared via the rapid combustion process. *J. Alloys Compd*. **2021**, 885, 160969. DOI: 10.1016/j.jallcom.2021.160969.
17. Zhu, H.L.; Luo, W.; Ciesielski, P.N.; Fang, Z.Q.; Zhu, J.Y.; Henriksson, G.; Himmel, M.E.; Hu, L.B. Wood-Derived Materials for Green Electronics, Biological Devices. and Energy Applications. *Chem. Rev*. **2016**, 116, 9305-9374. DOI: 10.1021/acs.chemrev.6b00225.
18. Rinaldi, R.; Jastrzebski, R.; Clough, M.T.; Ralph, J.; Kennema, M.; Bruijnincx, P.C.A.; Weckhuysen, B.M. Paving the Way for Lignin Valorisation: Recent Advances in Bioengineering, Biorefining and Catalysis. *Angew. Chem. Int. Ed*. **2016**, 55, 8164-8215. DOI: 10.1002/anie.201510351.
19. Thakur, V.K.; Thakur, M.K.; Raghavan, P.; Kessler, M.R. Progress in Green Polymer Composites from Lignin for Multifunctional Applications: A Review. *ACS Sustainable Chem. Eng*. **2014**, 2, 1072-1092. DOI: 10.1021/sc500087z.
20. Lora1, J.H.; Glasser, W.G. Recent Industrial Applications of Lignin: A Sustainable Alternative to Nonrenewable Materials. *J. Polym. Environ*. **2002**, 10, 39-48. DOI: 10.1023/A:1021070006895.
21. Dawy, M.; Shabaka, A.A.; Nada, A.M.A. Molecular structure and dielectric properties of some treated lignins. *Polym. Degrad. Stab*. **1998**, 62, 455-462. DOI: 10.1016/S0141-3910(98)00026-3.
22. Du, X.Y.; Li, J.B.; Lindström, M.E. Modification of industrial softwood kraft lignin using Mannich reaction with and without phenolation pretreatment. *Ind. Crops Prod*. **2014**, 52, 729-735. DOI: 10.1016/j.indcrop.2013.11.035.
23. Chen, H.; Liu, T.L.; Meng, Y.; Cheng, Y.; Lu, J.; Wang, H.S. Novel graphene oxide/aminated lignin aerogels for enhanced adsorption of malachite green in wastewater. *Colloids Surf. A Physicochem. Eng. Asp*. **2020**, 603, 125281. DOI: 10.1016/j.colsurfa.2020.125281.
24. An, L.; Si, C.L.; Bae, J.H.; Jeong, H.; Kim, Y.S. One-step silanization and amination of lignin and its adsorption of Congo red and Cu (II) ions in aqueous solution. *Int. J. Biol. Macromol*. **2020**, 159, 222-230. DOI: 10.1016/j.ijbiomac.2020.05.072.
25. Shah, M.M.; Grover, T.A.; Barr, D.P.; Aust, S.D. On the mechanism of inhibition of the veratryl alcohol oxidase activity of lignin peroxidase $H_2$ by EDTA. *J. Biol. Chem*. **1992**, 267, 21564-21569. DOI: 10.1016/0014-5793(92)81127-8.

26. Meng, X.Z.; Scheidemantle, B.; Li, M.; Wang, Y.Y.; Zhao, X.H.; Toro-Gonzalez, M.; Singh, P.; Pu, Y.Q.; Wyman, C. E.; Ozcan, S.; Cai, C.M.; Ragauskas, A.J. Synthesis, Characterization, and Utilization of a Lignin-Based Adsorbent for Effective Removal of Azo Dye from Aqueous Solution. *ACS omega*. **2020**, 5, 2865-2877. DOI: 10.1021/acsomega.9b03717.
27. Wang, Y.Y.; Zhu, L.L.; Wang, X.H.; Zheng, W.R.; Hao, C.; Jiang, C.L.; Wu, J.B. Synthesis of aminated calcium lignosulfonate and its adsorption properties for azo dyes. *J. Ind. Eng. Chem*. **2018**, 61, 321-330. DOI: 10.1016/j.jiec.2017.12.030.
28. Wang, X.H.; Zhang, Y.K.; Hao, C.; Dai, X.H.; Zhou, Z.L.; Si, N.C. Ultrasonic-assisted synthesis of aminated lignin by a Mannich reaction and its decolorizing properties for anionic azo-dyes, *RSC Adv*. **2014**, 4, 8156-28164. DOI: 10.1039/c4ra03133d.
29. Zhang, B.P.; Zhang, H.; Wang, Y.; Fang, S.Y. Adsorption behavior and mechanism of amine/quaternary ammonium lignin on tungsten. *Int. J. Biol. Macromol*. **2022**, 216, 882-890. DOI: 10.1016/j.ijbiomac.2022.07.226.
30. Pan, H.; Sun, G.; Zhao, T. Synthesis and characterization of aminated lignin. *Int. J. Biol. Macromol*. **2013**, 59, 221-226. DOI: 10.1016/j.ijbiomac.2013.04.049.
31. Vargas, A.M.M.; Cazetta, A.L.; Kunita, M.H.; Silva, T.L.; Almeida, V.C. Almeida Adsorption of methylene blue on activated carbon produced from flamboyant pods (Delonix regia): Study of adsorption isotherms and kinetic models. *Chem. Eng. J*. **2011**, 168, 722-730. DOI: 10.1016/j.cej.2011.01.067.
32. Le, G.T.T.; Chanlek, N.; Manyam, J.; Opaprakasit, P.; Grisdanurak, N.; Sreearunothai, P. Insight into the ultrasonication of graphene oxide with strong changes in its properties and performance for adsorption applications. *Chem. Eng. J*. **2019**, 373, 1212-1222. DOI: 10.1016/j.cej.2019.05.108.
33. Farias, R.S.; Buarque, H.L.D.; Cruz, M.R.; Cardoso, L.M.F.; Gondim, T.D.; Paulo, V.R. Adsorption of congo red dye from aqueous solution onto amino-functionalized silica gel. *Eng. Sanit. e Ambient*. **2018**, 23, 1053-1060. DOI: 10.1590/S1413-41522018172982.
34. Silva, M.M.F.; Oliveira, M.M.; Avelino, M.C.; Fonseca, M.G.; Almeida, R.K.S.; Silva, E.C. Adsorption of an industrial anionic dye by modified-KSF-montmorillonite: Evaluation of the kinetic. thermodynamic and equilibrium data. *Chem. Eng. J*. **2012**, 203, 259-268. DOI: 10.1016/j.cej.2012.07.009.
35. Radoor, S.; Karayil, J.; Jayakumar, A.; Nandi, D.; Parameswaranpillai, J.; Lee, J.; Shivanna, J.M.; Nithya, R.; Siengchin, S. Adsorption of Cationic Dye onto ZSM-5 Zeolite-Based Bio Membrane: Characterizations, Kinetics and Adsorption Isotherm. *J. Polym. Environ*. **2022**, 30, 3279-3292. DOI: 10.1007/s10924-022-02421-5.
36. Tseng, R.L.; Wu, F.C.; Juang, R.S. Characteristics and applications of the Lagergren's first-order equation for adsorption kinetics. *J. Taiwan Inst. Chem Eng*. **2010**, 41, 661-669. DOI: 10.1016/j.jtice.2010.01.014.
37. Mahmoodi, N.M.; Taghizadeh, M.; Taghizadeh, A.; Abdi, J.; Hayati, B.; Shekarchi, A.A. Bio-based magnetic metal-organic framework nanocomposite: Ultrasound-assisted synthesis and pollutant (heavy metal and dye) removal from aqueous media. *Appl. Surf. Sc*i. **2019**, 480, 288-299. DOI: 10.1016/j.apsusc.2019.02.211.
38. Azimi, E.B.; Badiei, A.; Ghasemi, J.B. Efficient removal of malachite green from wastewater by using boron-doped mesoporous carbon nitride. *Appl. Surf. Sci*. **2019**, 469, 236-245. DOI: 10.1016/j.apsusc.2018.11.017.
39. Ho, Y.S.; McKay, G. The kinetics of sorption of divalent metal ions onto sphagnum moss peat. *Water Res*. **2000**, 34, 735-742. DOI: 10.1016/s0043-1354(99)00232-8.
40. Cai, W.Q.; Tan, L.J.; Yu, J.G.; Jaroniec, M.; Liu, X.Q.; Cheng, B.; Verpoort, F. Synthesis of amino-functionalized mesoporous alumina with enhanced affinity towards Cr (VI) and $CO_2$. *Chem. Eng. J*. **2014**, 239, 207-215. DOI: 10.1016/j.cej.2013.11.011.
41. Malkoc, E.; Nuhoglu, Y.; Dunda, M. Adsorption of chromium (VI) on pomace-An olive oil industry waste: Batch and column studies. *J. Hazard. Mater*. **2006**, 138, 142-151. DOI: 10.1016/j.jhazmat.2006.05.051.
42. Li, Z.C.; Hanafy, H.; Zhang, L.; Sellaoui, L.; Netto, M.S.; Oliveira, M.L.S.; Seliem, M.K.; Dotto, G.L.; Bonilla-Petriciolet, A.Li,Q. Adsorption of congo red and methylene blue dyes on an ashitaba waste and a walnut shell-based activated carbon from aqueous solutions: Experiments, characterization and physical interpretations. *Chem. Eng. J*. **2020**, 388, 124263. DOI: 10.1016/j.cej.2020.124263.
43. Raji, F.; Pakizeh, M. Study of Hg (II) species removal from aqueous solution using hybrid $ZnCl_2$ -MCM-41 adsorbent. *Appl. Surf. Sci*. **2013**, 282, 415-424. DOI: 10.1016/j.apsusc.2013.05.145.
44. Bera, A.; Kumar, T.; Ojha, K.; Mandal, A. Adsorption of surfactants on sand surface in enhanced oil recovery: Isotherms, kinetics and thermodynamic studies. *Appl. Surf. Sc*i. **2013**, 284, 87-99. DOI: 10.1016/j.apsusc.2013.07.029.
45. Satapathy, M.K.; Das, P. Optimization of crystal violet dye removal using novel soil-silver nanocomposite as nanoadsorbent using response surface methodology. *J. Environ. Chem. Eng*. **2014**, 2, 708-714. DOI: 10.1016/j.jece.2013.11.012.
46. Sari, A.; Mendil, D.; Tuzena, M.; Soylak, M. Biosorption of palladium (II) from aqueous solution by moss (Racomitrium lanuginosum) biomass: Equilibrium, kinetic and thermodynamic studies. *J. Hazard. Mater*. **2009**, 162, 874-879. DOI: 10.1016/j.jhazmat.2008.05.112.

 doi:10.20944/preprints202311.1344.v1



disclaim responsibility for any injury to people or property resulting from any ideas, methods, instructions or products referred to in the content.